A Nonparabolicity Model Compared to Tight-Binding: The Case of Square Silicon Quantum Wires

A. Esposito [a,*] , M. Luisier [b], M. Frey [a], A. Schenk [a]

[a] *Integrated Systems Laboratory, ETH Zurich, Gloriastrasse 35, CH-8092, Switzerland*

[b] *Network for Computational Nanotechnology, Purdue University, 465 Northwestern Avenue, West Lafayette IN 47907, USA*

Abstract

This work presents a nonparabolicity (NP) model which is able to improve the effective mass approximation (EMA) for computing transfer characteristics of square silicon quantum wire transistors (SQWT) working in the ballistic regime and subjected to bandstructure effects. The model is found to be treatable within the same transport framework as used in a present 3D EMA Poisson-Schrödinger solver thus keeping a comparable time efficiency. A full-band tight-binding (TB) code provides the bandstructures as well as the transfer characteristics related to a series of SQWTs needed for calibrating the NP model. In comparison with the EMA, the threshold voltage (V_{T}) obtained via the NP model is notably closer to the TB data for all wire widths considered in this work. In addition, the NP model is found to satisfactorily predict the increase of the conduction masses belonging to the unprimed conduction valleys of the TB bandstructure.

Key words: Nonparabolicity; Quantum Wires; Tight-Binding; Ballistic Transport

1. Introduction

The effective mass approximation [1] (EMA) always provides a good starting point for the quantum mechanical treatment of charge transport in electronic devices [4]. The full Schrödinger problem describing the device at an atomic level is considerably simplified by circumventing the crystal potential term at the cost of a slightly modified kinetic operator. However, the EMA is intended for problems whose external perturbations are smooth compared to the lattice constant of the considered material. Thus, for devices involving confinements down to the nanometer length scale the EMA becomes questionable. A remedy is provided by more advanced methods [2,9–11] which consider the atomistic nature of the material thus being more precise than the single band picture of the EMA. On the other hand, the gain in precision of an atomistic simulation goes at the expense of the simulation time which increases significantly. The investigation of bandstructure effects and consequently the suitability of envelope approximations is therefore a major task in the development of nowadays nanoscale quantum transport simulators. Several efforts have been made in order to investigate such effects in silicon quantum wire transistors (SQWT) using 1D semiclassical approaches [13,16] as well as 3D simulations within a full quantum transport framework [12,15]. Beyond the manipulation of masses and band edges within the EMA also truncated nonparabolic dispersions along the transport direction [17] have been studied in order to account for bandstructure effects.

In this work the attention is restricted to the ballistic treatment of square SQWTs having a channel grown in the $\langle 100 \rangle$ direction and known to reside in

* Corresponding author. Tel.: +41 44 632 7580; Fax: +41 44 632 1194.

Email address: esposito@iis.ee.ethz.ch (A. Esposito).

a regime where bandstructure effects become important. A nonparabolicity (NP) model is introduced and discussed which is capable to improve the EMA for computing the currents in this regime. The nonparabolic portion of the Hamiltonian is fully taken in account by means of a suitable basis expansion. For the calculation of both EMA and NP transfer characteristics the 3D Poisson-Schrödinger solver SIMNAD [5] is used. Given a fixed device configuration, i.e. wire width, the characteristics and bandstructures are first computed via a full-band tight-binding (TB) code [2] which serve as a reference. The NP model is parametrized according to the corresponding TB bandstructure and the resulting threshold voltage (V_{T}) is finally compared to the TB data in order to quantify the improvement compared to the EMA. This procedure is repeated for a distinct set of wire widths while the TB formalism is always assumed to properly describe the bandstructure effects.

In Sec. 2 a detailed survey on the solution of the EMA Schrödinger equation with open boundary conditions as implemented in SIMNAD is given for the case of quantum wires. Further details on the current computation [4] as well as the iteration scheme for the self-consistency [6] are not given in this work. The framework is used in Sec. 3 in order to explain the implementation of the NP model whereas the comparison with the TB results and related discussions are given in Sec. 4.

2. Schrödinger Equation with Open Boundary Conditions

2.1. *The Transfer Matrix Approach*

As the Hamiltonian of an open quantum system possesses a continuous spectrum, the corresponding Schrödinger Equation needs not to be treated as an eigenvalue problem. Instead, it is possible to select an energy which is known to reside in the spectrum of the Hamiltonian and solve the Schrödinger equation as a boundary value problem. In this work, the attention is restricted to a rectangular simulation domain

$$\vec{r} = (x, y, z) \in [0, L_x] \times [0, L_y] \times [0, L_z] \tag{1}$$

containing silicon grown in the $\langle 100 \rangle$ direction. The corresponding EMA envelope equation has the form

$$\left(-\frac{\hbar^2}{2} \nabla \, \widehat{\mathbf{m}^{-1}} \, \nabla + V(\vec{r}) - E \right) \Psi(\vec{r}) = 0, \tag{2}$$

where $V(\vec{r})$ denotes the sum of the electrostatic potential and the geometric confinement and $\{1/m_x, 1/m_y, 1/m_z\}$ are the diagonal entries of $\widehat{\mathbf{m}^{-1}}$. In the case of quantum wires having a channel along the x-direction one might apply the boundary conditions

$$\Psi(0, y, z) = f(y, z) \tag{3}$$

$$\frac{\partial}{\partial x} \Psi(\vec{r})|_{\vec{r}=(0,y,z)} = g(y, z) \tag{4}$$

$$\Psi|_{y=0} = \Psi|_{y=L_y} = \Psi|_{z=0} = \Psi|_{z=L_z} = 0 \tag{5}$$

for two given functions $f, g : [0, L_y] \times [0, L_z] \to \mathbb{C}$. The problem stated in Eqs. (2), (3), (6), and (5) can be solved via the transfer matrix method. For this purpose the transport direction x is subdivided in $N + 1$ intervals

$$\mathbf{I}(x, n, N) \equiv \begin{cases} [x_0, (x_0 + x_1)/2], & n = 0 \\ [(x_{N-1} + x_N)/2, x_N], & n = N \\ [(x_{n-1} + x_n)/2, (x_n + x_{n+1})/2], & \text{otherwise} \end{cases} \tag{6}$$

for a given set of points $\{x_n \mid 0 = x_0 < x_1 < \ldots < x_{N-1} < x_N = L_x\}$. The external potential $V(\vec{r})$ from Eq. (2) is assumed to be piecewise constant along the transport direction, i.e. approximated by $U_n(y, z) \equiv V(x_n, y, z)$ on the interval $\mathbf{I}(x, n, N)$. By means of the ansatz

$$\Psi(\vec{r})|_{x \in \mathbf{I}(x,n,N)} = \exp(\pm i k_i^n x) \Phi_i^n(y, z) \tag{7}$$

on $\mathbf{I}(x, n, N)$, the Schrödinger problem given in Eq. (2) reduces to a transverse equation of the form

$$\widehat{\mathbf{H}}_n \Phi_i^n(y, z) = \underbrace{\left(E - \frac{(\hbar k_i^n)^2}{2 m_x} \right)}_{\epsilon_i^n} \Phi_i^n(y, z) \tag{8}$$

with

$$\widehat{\mathbf{H}}_n \equiv \left[-\frac{\hbar^2}{2} \left(\frac{\partial}{\partial y} \frac{1}{m_y} \frac{\partial}{\partial y} + \frac{\partial}{\partial z} \frac{1}{m_z} \frac{\partial}{\partial z} \right) + U_n(y, z) \right].$$

The discrete eigenvalues ϵ_i^n rising from the transverse problem given in Eq. (8) are referred to as the subband energies and enter the wavenumber k_i^n from Eq. (7) together with the total energy E yielding

$$k_i^n = \begin{cases} \dfrac{\sqrt{2 m_x (E - \epsilon_i^n)}}{\hbar}, & E - \epsilon_i^n \geq 0 \\ i \dfrac{\sqrt{2 m_x (\epsilon_i^n - E)}}{\hbar}, & \text{otherwise.} \end{cases}$$

Finally, the total wave function $\Psi(\vec{r})$ to a given energy E has the form

$$\Psi(\vec{r}) = \sum_{n=0}^{N} \chi_n(x) \sum_{i\in\Lambda} \{a_i^n \exp[ik_i^n(x-x_n)] + b_i^n \exp[-ik_i^n(x-x_n)]\}\Phi_i^n(y,z), \quad (9)$$

where $\chi_n(x)$ is the characteristic function on $\mathbf{I}(x,n,N)$ and Λ is the set of transverse quantum numbers i. The degrees of freedom $\{a_i^n,\ b_i^n \mid i \in \Lambda;\quad n = 0,\ldots,N\}$ from Eq. (9) are reduced by requiring the continuity of Ψ and $(1/m_x)(\partial/\partial x)\Psi$ at the transitions between two adjacent intervals $\mathbf{I}(x,n,N)$ and $\mathbf{I}(x,n+1,N)$. The remaining coefficients $\{a_i^0\}_{i\in\Lambda}$ and $\{b_i^0\}_{i\in\Lambda}$ are finally fixed by the functions f and g from Eqs. (3) and (6). Further details concerning the numerics can be found in Ref. [4].

2.2. *Solution of the Transverse Problem*

A possible scheme for solving the two-dimensional Schrödinger problem stated in Eq. (8) on a rectangular domain subjected to Dirichlet boundary conditions is provided by a standard finite difference (FD) scheme. For this purpose the domain can be meshed according to a tensorial grid parametrized by means of two sets of points $\{y_j \mid j = 0,\ldots,J\}$ and $\{z_k \mid k = 0,\ldots,K\}$ as illustrated in Fig. 1 with corresponding intervals $\mathbf{I}(y,j,J)$ and $\mathbf{I}(z,k,K)$ according to Eq. (6). A further scheme is provided by an expansion of the solution Φ^n in terms of a suitable basis set in analogy to Ref. [3]. For this purpose the transverse potential $U_n(y,z)$ from Eq. (8) is sampled at the positions (y_j,z_k) yielding $U_{jk} \equiv U(y_j,z_k)$. A representation of $U_n(y,z)$ defined all over the simulation domain is given by a stepwise constant function

$$U_n(y,z) = \sum_{j=0}^{J}\sum_{k=0}^{K} U_{jk}\chi_{jk}(y,z), \quad (10)$$

where $\chi_{jk}(y,z)$ is the characteristic function on the interval $\mathbf{I}(y,j,J) \times \mathbf{I}(z,k,K)$. A possible position dependency of the transverse effective masses $m_y \to m_y(x_n,y,z)$ and $m_z \to m_z(x_n,y,z)$ from Eq. (8) can be treated in the same way as for $U_n(y,z)$ in Eq. (10). In a next step the solution $\Phi^n(y,z)$ from Eq. (8) is expanded in terms of sine waves

$$\Phi^n(y,z) = \sum_{r=1}^{R}\sum_{s=1}^{S} c_{rs}^n \langle y,z|r,s\rangle \equiv \frac{2}{\sqrt{L_yL_z}} \sum_{r=1}^{R}\sum_{s=1}^{S} c_{rs}^n \sin\left(y\frac{r\pi}{L_y}\right)\sin\left(z\frac{s\pi}{L_z}\right), \quad (11)$$

where $R,S \in \mathbb{N}$ denote cutoffs. Note that the sine waves from Eq. 11 are orthonormal with respect to the simulation domain $L_y \times L_z$, i.e.

$$\begin{aligned}\langle r',s'|r,s\rangle &\equiv \frac{4}{L_yL_z}\int_0^{L_y}\int_0^{L_z} \sin\left(y\frac{r'\pi}{L_y}\right)\sin\left(z\frac{s'\pi}{L_z}\right) \\ &\quad\times \sin\left(y\frac{r\pi}{L_y}\right)\sin\left(z\frac{s\pi}{L_z}\right)dydz \\ &= \delta_{r,r'}\delta_{s,s'} \end{aligned} \quad (12)$$

and naturally include Dirichlet conditions at the boundaries. Using the ansatz from Eq. (11) for the problem stated in Eq. (8) yields an algebraic eigenvalue problem of the form

$$\mathbf{H}_n\mathbf{c}_n = \epsilon_n\mathbf{c}_n, \quad (13)$$

where the vector $\mathbf{c}_n$ and the matrix $\mathbf{H}_n$ are given by

$$\begin{aligned}&\mathbf{H}_n(r's',rs) \equiv \langle r',s'|\widehat{\mathbf{H}}_n|r,s\rangle \\ &= \frac{4}{L_yL_z}\int_0^{L_y}\int_0^{L_z} \sin\left(y\frac{r'\pi}{L_y}\right)\sin\left(z\frac{s'\pi}{L_z}\right) \\ &\times\widehat{\mathbf{H}}_n \sin\left(y\frac{r\pi}{L_y}\right)\sin\left(z\frac{s\pi}{L_z}\right)dydz \end{aligned} \quad (14)$$

and $\mathbf{c}_n(rs) = c_{rs}$, respectively. The solution of the algebraic problem given in Eq. (13) yields the desired eigenvectors $\Phi_i^n(y,z)$ as well as the corresponding eigenenergies ϵ_i^n which are both labeled by the transverse quantum number i. As the attention is restricted to square quantum wires the cutoffs from Eq. (11) are both set to a common value C, i.e. $R = S = C$.

2.3. *Comparison of the Solution Schemes*

In order to compare the sine wave expansion (SE) method described in Eqs. (11) and (13) to a standard FD scheme the two-dimensional test framework described in Fig. 2 is considered. The model mimics a $D \times D$ silicon core region grown along the $\langle 100\rangle$ direction surrounded by a 1nm thick SiO2 layer, i.e. the dark area. The discontinuity at the Si/SiO2 interface is set to 3eV and the total potential enters the Schrödinger problem given in Eq. (8) via $U_n(y,z)$. The effective masses are set to $\{m_y,m_z\} = \{0.19m_e, 0.91m_e\}$ in the silicon and $\{m_y,m_z\} =$

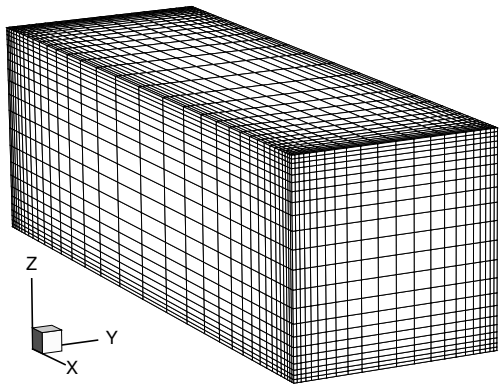

Fig. 1. Schematic representation of a tensorial grid discretization in three dimensions as used in Sec. 2.2.

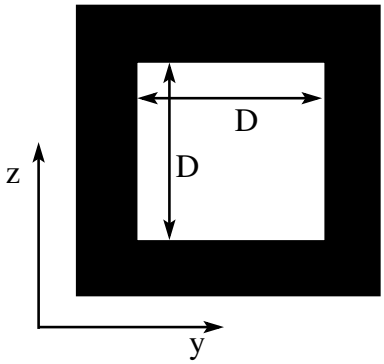

Fig. 2. A test framework used for the comparison between the SE method described in Eqs. (11) and (13) and a standard FD scheme.

$\{0.3m_e, 0.3m_e\}$ in the oxide where m_e is the electron mass. For $D \in \{2\text{nm}, 4.7\text{nm}\}$ the lowest five eigenvalues calculated via the SE method for $C = 30$ are compared to the ones obtained via the FD scheme and listed in Table 1, where a uniform grid of 101×101 points is used. The ground state energies differ by up to 3meV. In addition, the case of an infinitely high oxide barrier (∞) for D=2nm is presented showing the relevancy of the density penetration in the oxide. In the following a fixed cutoff of $C = 30$ is used and the penetration in the oxide is neglected in order to be as consistent as possible with the TB model [14,2].

Table 1
The Schrödinger problem given in Eq. 8 is applied to the test framework described in Fig. 2, where the Si/SiO2 barrier is set to 3eV. Shown are the lowest five eigenvalues in eV for $D \in \{2\text{nm}, 4.7\text{nm}\}$ calculated via the SE method as well as the FD scheme. Furthermore, the case of an infinitely high oxide barrier (∞) for D=2nm is presented showing the relevancy of the density penetration in the oxide.

SE(2nm)	FD(2nm)	∞(2nm)	SE(4.7nm)	FD(4.7nm)
0.3760	0.3730	0.5981	0.0866	0.0860
0.6533	0.6461	0.9080	0.1398	0.1386
1.1069	1.0924	1.4245	0.2283	0.2259
1.2326	1.2265	2.0824	0.2936	0.2920
1.5286	1.5181	2.1477	0.3474	0.3452

3. Nonparabolicity Model

3.1. *Motivation*

The EMA mainly relies on the assumption [1] that the confining potential which is superposed to the crystal structure varies slowly with respect to corresponding lattice constant. Furthermore, the wavefunction of the original problem is assumed to be well described within a single energy band of the crystal bandstructure, i.e. the silicon conduction band in this case. By reducing the width of a quantum wire the EMA is therefore expected to increasingly fail in reproducing results obtained via a more advanced scheme such as the TB [2] formalism. Sticking to the single band picture, a modification of the EMA is provided by nonparabolic [7,8] dispersions such as

$$(E - \epsilon_c)[1 + \alpha(E - \epsilon_c)] \equiv \frac{\hbar^2}{2} \vec{k}\, \widehat{\mathbf{m}^{-1}}\, \vec{k} \tag{15}$$

and consequently

$$E(\vec{k}) = \frac{1}{2\alpha}\left[\sqrt{1 + 4\alpha\frac{\hbar^2}{2}\vec{k}\, \widehat{\mathbf{m}^{-1}}\, \vec{k}} - 1\right] + \epsilon_c, \tag{16}$$

where α is referred to as the nonparabolicity coefficient having the dimension of an inverse energy and ϵ_c=1.12eV. The corresponding kinetic operator is obtained by replacing $\vec{k}$ with $-i\vec{\nabla}$ yielding a Schrödinger equation of the form

$$\left[\frac{1}{2\alpha}\left(\sqrt{1 - 4\alpha\frac{\hbar^2}{2}\nabla\, \widehat{\mathbf{m}^{-1}}\, \nabla} - 1\right) + \epsilon_c + U(\vec{r})\right]\Psi(\vec{r}) = \epsilon\Psi(\vec{r}). \tag{17}$$

Note that Eq. (17) can not be straightforwardly solved within the transfer matrix framework presented in Sec. 2 as the derivatives $\{\partial/\partial x, \partial/\partial y, \partial/\partial z\}$ couple to each other either via a general effective mass tensor or through the square root.

3.2. *Recovery of the transfer matrix formalism*

The impact of Eq. (17) on an one-dimensional electron gas (1DEG) [8] is investigated by means of the simple model potential

$$U(\vec{r}) = U(y,z) = \begin{cases} 0, & (y,z) \in [0,D]^2 \\ \infty, \text{ otherwise} \end{cases} . \tag{18}$$

The energy spectrum belonging to the Schrödinger problem described in Eqs. (17) and (18) in the case of a diagonal effective mass tensor $\widehat{\mathbf{m}^{-1}}$ such as in Sec. (2.1) is given by

$$\epsilon(n,m,k_x,\alpha) \equiv \frac{1}{2\alpha}\left[\sqrt{1+4\alpha\left(\epsilon_\parallel+\epsilon_\perp\right)}-1\right]+\epsilon_c \tag{19}$$

with $n,m = 1,2,\ldots$, $\epsilon_\parallel(k_x) \equiv \hbar^2 k_x^2/(2m_x)$, and $\epsilon_\perp(n,m) \equiv \hbar^2\pi^2(n^2/m_y + m^2/m_z)/(2D^2)$. In the case of a 1DEG one can intuitively make the assumption that $\epsilon_\parallel \ll \epsilon_\perp$ and consequently

$$\epsilon(n,m,k_x,\alpha) = \frac{1}{2\alpha}\left[\sqrt{1+4\alpha\epsilon_\perp}-1\right]+\epsilon_c + \frac{\epsilon_\parallel}{\sqrt{1+4\alpha\epsilon_\perp}} + O\left[\left(\frac{\epsilon_\parallel}{\epsilon_\perp}\right)^2\right]. \tag{20}$$

With the abbreviations $\beta(\alpha,\epsilon_\perp) \equiv \sqrt{1+4\alpha\epsilon_\perp}$ and $\epsilon^{\mathrm{NP}}(n,m,\alpha) \equiv \left[\sqrt{1+4\alpha\epsilon_\perp}-1\right]/(2\alpha)+\epsilon_c$ the spectrum given in Eq. (20) can be approximated by

$$\epsilon(n,m,k_x,\alpha) \simeq \epsilon^{\mathrm{NP}}(n,m,\alpha) + \frac{\epsilon_\parallel}{\beta(\alpha,\epsilon_\perp)}. \tag{21}$$

In the following $\beta_c \equiv \beta[\alpha,\epsilon_\perp(1,1)]$ and $\epsilon_c^{\mathrm{NP}} \equiv \epsilon^{\mathrm{NP}}(1,1,\alpha)$ will be used, where the α is omitted for simplicity. An interesting result is given by the second term on the right hand side of Eq. (21). The mass m_x is effectively renormalized (increased) due to the lateral confinement according to

$$m_x \rightarrow m_x\beta(\alpha,\epsilon_\perp). \tag{22}$$

In particular, β_c is related to the increase of m_x at the conduction band edge ϵ_c^{NP}. Similar results have already been obtained [12,13] in SQWTs. Based on Eq. (21) a simplified kinetic operator which describes the conduction band and fits in the scattering matrix formalism is given by

$$\frac{\hbar^2}{2\widetilde{m}_x}\frac{\partial^2}{\partial x^2} + \epsilon_c + \frac{1}{2\alpha}\left[\sqrt{1-4\alpha\frac{\hbar^2}{2}\left(\frac{1}{m_y}\frac{\partial^2}{\partial y^2}+\frac{1}{m_z}\frac{\partial^2}{\partial z^2}\right)}-1\right] \tag{23}$$

where α and the conduction mass $\widetilde{m}_x$ are given for a fixed width D. Dispersions including nonparabolicity only in the transverse direction have already been used [3] in order to selfconsistently compute charge densities. Note that the change of the operator ordering in Eq. (23) compared to Eq. (8) is justified by the requirement that $\{m_x, m_y, m_z\}$ are position independent as it assumed for the rest of the work. Furthermore, the conduction mass $\widetilde{m}_x$ can be set to values other than $\beta_c m_x$. The Hamiltonian from Eq. (8) finally becomes

$$\widehat{\mathbf{H}}_n^{\mathrm{NP}} \equiv \frac{1}{2\alpha}\left[\sqrt{1-4\alpha\frac{\hbar^2}{2}\left(\frac{1}{m_y}\frac{\partial^2}{\partial y^2}+\frac{1}{m_z}\frac{\partial^2}{\partial z^2}\right)}-1\right] + U_n(y,z), \tag{24}$$

where ϵ_c is absorbed in U_n.

3.3. *Extraction of α and $\widetilde{m}_x$*

In order to determine a suitable NP coefficient α and a renormalized conduction mass $\widetilde{m}_x$ related to the square silicon quantum wires (SSQW) considered in this work a direct comparison with the TB formalism is necessary. For this purpose, the bandstructures belonging to SSQWs having a channel grown along the $\langle 100\rangle$ direction are computed via the TB [2] code for a distinct set of wire widths $D[\mathrm{nm}] \in \{2.04, 2.44, 2.85, 3.26, 3.53, 3.94, 4.34, 4.75\}$. Further details concerning the TB termination model at the Si surface can be found in Ref. [14]. Figure 3 shows the TB bandstructure for the widths $D[\mathrm{nm}] \in \{2.04, 4.75\}$ together with the dispersions $\epsilon_c^{\mathrm{NP}} + \epsilon_\parallel/\beta_c$ from Eq. (21) for one of the four unprimed valleys Δ_4, i.e. $(m_x,m_y,m_z)/m_e = (0.19, 0.91, 0.19)$. Note the difference to the case $\beta_c \equiv 1$ which corresponds to the EMA up to a shift along the energy axis. The corresponding NP coefficient α which enters β_c as well as ϵ_c^{NP} is determined via $\epsilon_c^{\mathrm{NP}} - \epsilon_c^{\mathrm{TB}} = 0$, where ϵ_c^{TB} is the TB conduction band $E^{\mathrm{TB}}(k_x)$ evaluated at the Γ point, i.e. $k_x = 0$. A plot of α and the corresponding β_c as a function of the wire width is given in Fig. 4. Accordingly, Fig. 5 shows the band edge ϵ_c^{TB} and $\epsilon_c^{\mathrm{EMA}} \equiv \epsilon_c^{\mathrm{NP}}(\alpha \rightarrow 0\mathrm{eV}^{-1})$ as well as a comparison between the renormalized conduction masses $m_x\beta_c$

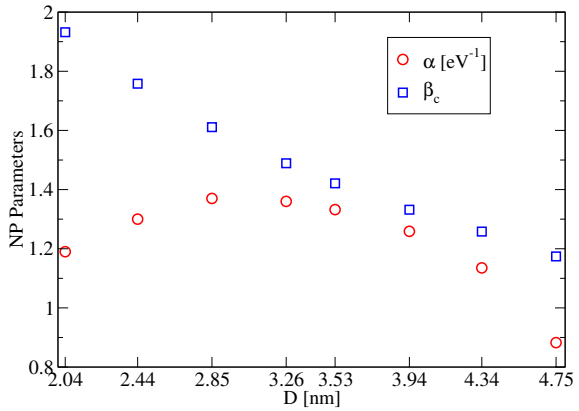

Fig. 4. The NP coefficient α determined by means of $\epsilon_c^{\mathrm{NP}} - \epsilon_c^{\mathrm{TB}} = 0$ together with the corresponding $\beta_c \equiv \beta[\alpha, \epsilon_\perp(1,1)]$ for each wire width D.

and extracted values $m_x^{\mathrm{TB}} \equiv \hbar^2/(\partial^2 E^{\mathrm{TB}}/\partial^2 k_x)$ at the Γ point. The $m_x\beta_c$ are found to be satisfactorily close to the m_x^{TB}. Note that the same α and $m_x\beta_c$ are obtained when the original $\epsilon(1,1,k_x,\alpha)$ from Eq. (19) is fitted to ϵ_c^{TB}.

According to the Δ_4 valleys, effective masses and energy minima can be extracted for one of the two primed valleys Δ_2 located at $k_x = \pm 0.336\pi/a$ of the TB bandstructure given in Fig. 3. As the masses belonging to the Δ_4 and Δ_2 valleys are related [12] to the bulk values $(m_t^{\mathrm{bulk}}, m_l^{\mathrm{bulk}})/m_e = (0.91, 0.19)$, respectively one obtains a corresponding set $\{m_l^{\mathrm{TB}}, m_t^{\mathrm{TB}}\}$ for each diameter D. Both m_t^{TB} as given in Fig. 5.a and m_l^{TB} (not reported in this work) are larger than the corresponding bulk values. The impact of larger masses on $\epsilon_c^{\mathrm{EMA}}$ is expected to be a reduction of $|\epsilon_c^{\mathrm{EMA}} - \epsilon_c^{\mathrm{TB}}|$ and therefore desirable. However, the set $\{m_l^{\mathrm{TB}}, m_t^{\mathrm{TB}}\}$ belonging to the present TB bandstructure leads to an unfavorable overstimation of ϵ_c^{TB} by $\epsilon_c^{\mathrm{EMA}}$ and prevents an extraction of α via $\epsilon_c^{\mathrm{NP}} - \epsilon_c^{\mathrm{TB}} = 0$ as explained in this section. The use of $\{m_y, m_z\}/m_e \in \{0.91, 0.19\}$ is therefore mandatory for the Hamiltonian given in Eq. (24) and a deviation from bulk effective masses within the EMA case is not considered in this work. Note that the splitting of the TB Δ_4 valleys due to the transverse confinement as shown in the inset of Fig. 3.a is not taken in to account in this work. Finally, the NP model is solely applied to the Δ_4 valleys and $\widetilde{m}_x = m_x\beta_c$ will be used for the rest of the work.

3.4. *Solution of the NP Problem*

In order to diagonalize the Hamiltonian given in Eq. (24) a special kind of kinetic operators

$$T(\widehat{O}) \equiv T\left[-\frac{\hbar^2}{2}\left(\frac{1}{m_y}\frac{\partial^2}{\partial y^2} + \frac{1}{m_z}\frac{\partial^2}{\partial z^2}\right)\right] \tag{25}$$

is considered, possessing a Taylor expansion

$$T(\widehat{O}) = \sum_{i=0}^{\infty} \frac{T^{(i)}(0)}{i!}\widehat{O}^n, \tag{26}$$

where $T^{(i)}$ is the i-th derivative of T. The matrix elements of $T(\widehat{O})$ in the sine wave basis from Eq. (11) can be computed analytically yielding

$$\langle r', s'|T(\widehat{O})|r, s\rangle = T\left[\frac{\hbar^2\pi^2}{2}\left(\frac{1}{m_y}\frac{r^2}{L_y^2} + \frac{1}{m_z}\frac{s^2}{L_z^2}\right)\right]\delta_{r,r'}\delta_{s,s'}. \tag{27}$$

Therefore, the SE method from Sec. 2 can be used in order to diagonalize the $\widehat{\mathbf{H}}_n^{\mathrm{NP}}$ from Eq. (24). It has to be noted that the flat potential in Eq. (18) is chosen in order to allow a comparison with the TB bandstructure and consequently the extraction of the NP coefficient as shown in Fig. 4. However, the justification of the simplified kinetic operator given in Eq. (23) is not restricted to the presence of a flat potential. This can be easily seen by considering a general transverse potential $U(y,z)$ including hard walls at the boundary and expanding the Hamiltonian given in Eq. (17) in terms of the set

$$\langle \vec{r}|k_x, n, m\rangle = A\exp(ik_x x)\sin\left(\frac{n\pi y}{D}\right)\sin\left(\frac{m\pi z}{D}\right), \tag{28}$$

where A is a normalization constant. The kinetic part is diagonal and proportional to

$$\left\{\frac{1}{2\alpha}\left[\sqrt{1 + 4\alpha\left(\epsilon_\parallel + \epsilon_\perp\right)} - 1\right] + \epsilon_c\right\} \delta_{n,n'}\delta_{m,m'}\delta(k_x - k_x'), \tag{29}$$

where $\epsilon_\parallel(k_x)$, $\epsilon_\perp(n,m)$, and $\widehat{\mathbf{m}^{-1}}$ are taken from Sec. 3.2. After assuming that in the presence of a strong transverse confinement the condition $\epsilon_\parallel \ll \epsilon_\perp$ holds for the relevant expansion coefficients related to $|k_x, n, m\rangle$ one can modify the matrix elements given in Eq. (29) according to Eq. (20). In particular, after appropriately replacing $\beta(\alpha, \epsilon_\perp)$ the matrix elements become identical to the ones obtained via the simplified kinetic operator given in

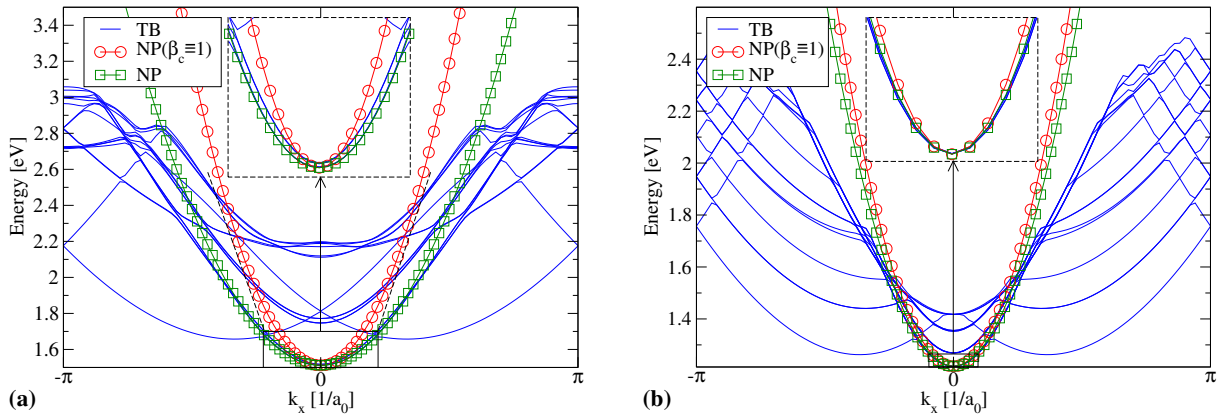

Fig. 3. TB dispersion relations for a square silicon nanowire grown along the ⟨100⟩ direction with widths (a) D=2.04nm and (b) D=4.75nm. The length of the wire unit cell is $a_0 = 0.543$nm. In addition, the dispersions $\epsilon_c^{\mathrm{NP}} + \epsilon_{\|}/\beta_c$ from Eq. (21) are plotted including the case $\beta_c \equiv 1$.

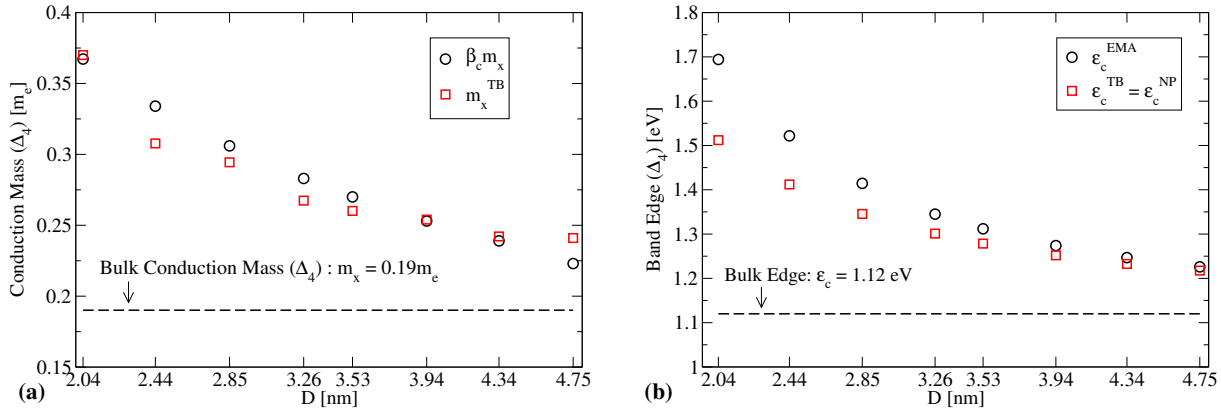

Fig. 5. (a) Renormalized conduction mass $m_x\beta_c$ compared to $m_x^{\mathrm{TB}} \equiv \hbar^2/(\partial^2 E^{\mathrm{TB}}/\partial^2 k_x)$ obtained via the TB conduction band $E^{\mathrm{TB}}(k_x)$ at the Γ point, i.e. $k_x = 0$. Data is given for a distinct set of widths D (b) Conduction band edges ϵ_c^{TB} and $\epsilon_c^{\mathrm{EMA}} \equiv \epsilon_c^{\mathrm{NP}}(\alpha \to 0\mathrm{eV}^{-1})$ as a function of the wire width. The condition $\epsilon_c^{\mathrm{NP}} = \epsilon_c^{\mathrm{TB}}$ holds for the set of coefficients α given in Fig. 4.

Eq. (23) thus justifying the form of the operator even in the presence of a general transverse potential $U(y, z)$.

4. Simulation Results

The suitability of the NP model presented in Sec. 3.2, i.e. the assumptions leading to Eq. (23), are quantitatively investigated by means of a comparison to transfer characteristics calculated via the TB framework [2]. The device of choice consists of a triple gate SQWT having a channel grown in the ⟨100⟩ direction as described in Fig. 6. The source and drain regions are n-doped with a concentration of $10^{20}\mathrm{cm}^{-3}$ and a fixed source-to-drain bias V_{DS} of 0.6V is applied. The currents are computed for a distinct set of wire widths D being identical to the one used in Sec. 3. Finally, the penetration of charge in the oxide is neglected during both NP and TB current calculations.

Table 2
Different set of parameters which enter the NP model described in Sec. 3. The resulting V_{T} are summarized in Fig. 7. In particular, set I is referred to as the EMA case and the notation $\alpha(D)$ refers to the NP coefficients plotted in Fig. 4.

	I	II	III
α	$0\mathrm{eV}^{-1}$	$\alpha(D)$	$\alpha(D)$
$\widetilde{m}_x$	$0.19m_e$	$0.19m_e\beta_c$	$0.19m_e$

A quantity which is suitable for the comparison of transfer characteristics is given by the threshold voltage V_{T} which is defined according to Ref.[13] via

$$I_{\mathrm{DS}}(V_{\mathrm{GS}} = V_{\mathrm{T}}, V_{\mathrm{DS}} = 0.6\mathrm{V}) = 300\mathrm{nA}, \qquad (30)$$

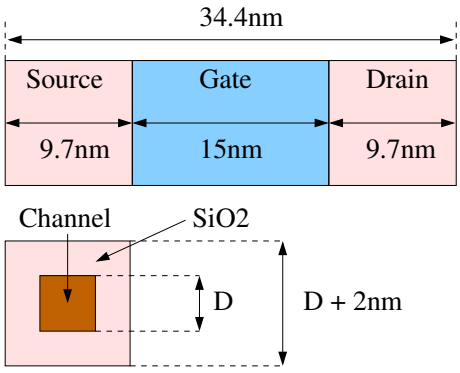

Fig. 6. Schematic representation of a triple gate silicon quantum wire having a channel grown in the ⟨100⟩ direction used for the comparisons in Sec. 4.

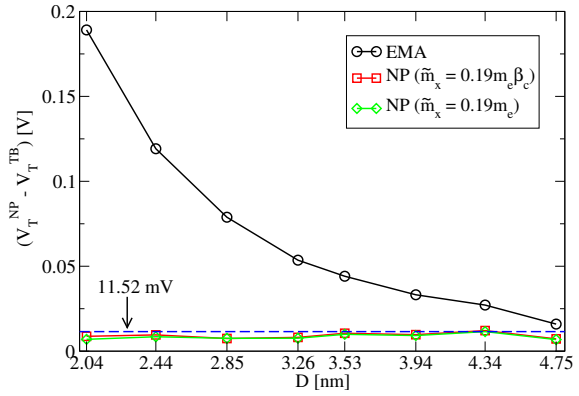

Fig. 7. (a) Dependence of the error $V_{\rm T}^{\rm NP} - V_{\rm T}^{\rm TB}$ on the wire width D. Plotted are the results obtained via the set of NP parameters summarized in Table 2. In particular, the squares and diamonds are for the same set of coefficients α whereas for the latter curve $\widetilde{m}_x = 0.19m_e$ has been used instead of $\widetilde{m}_x = 0.19m_e\beta_c$. The dashed line denotes the largest value of $V_{\rm T}^{\rm NP} - V_{\rm T}^{\rm TB}$.

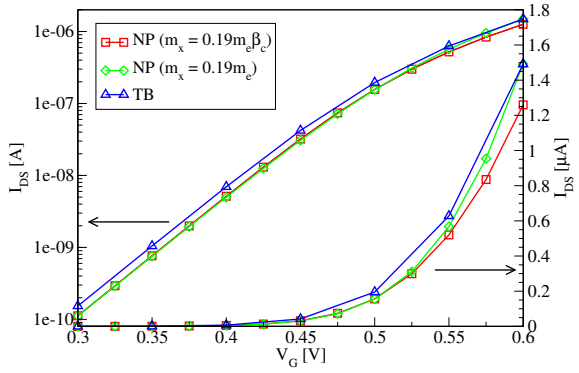

Fig. 8. Transfer characteristics of the structure described in Fig. 6 for a wire width $D = 2.04$nm. Shown are the results from the TB calculation as well as from set II and III given in Table 2.

where $I_{\rm DS}$ and $V_{\rm GS}$ denote the drain current and gate voltage, respectively. The $V_{\rm T}$ is computed for the set of parameters given in Table 2 and the corresponding results are summarized in Fig. 7. For the smallest wire widths the overestimation of $V_{\rm T}$ by set I, i.e. the EMA case, is quite notable. An substantial improvement is achieved by using II and III and note that the use of $\widetilde{m}_x = 0.19m_e$ has a minor impact on the calculation of the $V_{\rm T}$. Another bandstructure effect which is included in the NP model is related to the shift between $\epsilon_c^{\rm EMA}$ and $\epsilon_c^{\rm TB}$ as shown in Fig. 5. As the shift is comparable to the $V_{\rm T}$ overestimation it is assumed to be the main effect leading to the discrepancy manifested by set I. A similar observation has been reported for the case of cylindrical silicon nanowire transistors [17]. It has to be noted that only the Δ_4 valleys are modified as the difference after applying the NP model to either both Δ_4 and Δ_2 or to the Δ_4 valleys alone is found to be negligible.

Finally, the transfer characteristics belonging to the different parameterizations of Table 2 are summarized in Fig. 8 for the case of the smallest wire width $D = 2.04nm$. The current calculated via set II is slightly smaller compared to set III for large $V_{\rm GS}$ which can be related to the onset of tunneling currents being larger for smaller conduction masses. However, in the regime where the $V_{\rm T}$ is measured, the tunneling currents are assumed to be negligible as can be seen by the strong similarities between the outcomes of set II and III.

5. Conclusions

A suitable NP model is introduced which improves a present EMA quantum transport simulator for computing transfer characteristics by accounting for the main bandstructure effects appearing in SSQWs. In particular, the $V_{\rm T}$ belonging to a series of SSQW are computed via a full-band TB framework and the corresponding NP results are found to be notably closer to the TB data with respect to the EMA case. The calibration of the NP model relies upon the adjustment of a single coefficient which can be extracted from the corresponding TB bandstructure of the considered device. Consequently, the NP model includes the TB conduction band edge and is able to satisfactorily predict the increase of the conduction mass for the case of the unprimed valleys. A numerical solution of the problem is straightforward and the computational burden is comparable to the one caused by the EMA simula-

tor. In conclusion, this work is strongly focused on the technicalities of a newly introduced NP model while the application is preliminarily restricted to the V_{T} of SSQWs.

6. Acknowledgments

The authors are grateful for the financial support by the Swiss National Science Foundation (project NEQUATTRO SNF 200020-117613) and the European projects PULLNANO (IST-4-026828) and NANOSIL (IST-216171). Part of the simulation time has been provided by the NANOHUB project.

References

[1] Kohn W, Luttinger JM. Motion of Electrons and Holes in Perturbed periodic Fields. Phys. Rev. 1954; 97: 869-83.

[2] Luisier M, Schenk A, Fichtner W, Klimeck G. Atomistic simulation of nanowires in the $sp^3d^5s^*$ tight-binding formalism. Phys Rev B 2006; 74: 205323.

[3] Trellakis A, Ravaioli U. Three-dimensional spectral solution of the Schrödinger equation for arbitrary band structures. J Appl Phys 2002; 92: 3711-6.

[4] Heinz FO. Simulation Approaches for Nanoscale Semiconductor Devices. Konstanz: Hartung Gorre Verlag;
2004. Available: http://e-collection.ethbib.ethz.ch/cgi-bin/show.pl?type=diss&nr=15435

[5] Heinz FO, Schenk A. Self-consistent modeling of longitudinal quantum effects in nanoscale double-gate metal oxide semiconductor field effect transistors. J Appl Phys 2006; 100: 084314.

[6] Scholze A. Simulation of Single-Electron Devices. Konstanz: Hartung Gorre Verlag; 2000.

[7] López-Villanueva JA, Melchor I, Cartujo P, Carceller JE. Modified Schrödinger equation including nonparabolicity for the study of a two-dimensional electron gas. Phys Rev B 1993; 48: 1626-31.

[8] Godoy A, Yang Z, Ravaioli U, Gámiz F. Effects of nonparabolic bands in quantum wires. J Appl Phys 2005; 98: 013702.

[9] Delaney P, Greer JC. Correlated Electron Transport in Molecular Electronics. Phys Rev Lett 2004; 93: 036805.

[10] Albrecht M, Song B, Schnurpfeil A. A wave function based ab initio nonequilibrium Green's function approach to charge transport. J Appl Phys 2006; 100: 013702.

[11] Taylor J, Guo H, Wang J. Ab initio modeling of quantum transport properties of molecular electronic devices. Phys Rev B 2001; 63: 245407.

[12] Nehari K, Cavassilas N, Autran JL, Bescond M, Munteanu D, Lannoo M. Influence of band structure on electron ballistic transport in silicon nanowire MOSFET's: An atomistic study. Solid State Electronics 2006; 50: 716-21.

[13] Wang J, Rahman A, Ghosh A, Klimeck G, Lundstrom M. On the Validity of the Parabolic Effective-Mass Approximation for the I-V Calculation of Silicon Nanowire Transistors. IEEE Trans Electron Devices 2005; 52: 1589-95.

[14] Lee S, Oyafuso F, Von Allmen P, Klimeck G. Boundary conditions for the electronic structure of finite-extend embedded semiconductor nanostructures. Phys Rev B 2004; 69: 045316.

[15] Nehari K, Cavassilas N, Michelini F, Bescond M, Autran JL, Lannoo M. Full-band study of current across silicon nanowire transistors. Applied Physics Letters 2007; 90: 132112.

[16] Neophytou N, Paul A, Lundstrom MS, Klimeck G. Simulation of nanowire transistors: atomistic vs. effective mass models. J Comput Electron 2008; 7: 363-66.

[17] Gnani E, Reggiani S, Gnudi A, Parruchini P, Colle R, Rudan M, Baccarani G. Band-Structure Effects in Ultrascaled Silicon Nanowires. IEEE Trans Electron Devices 2007; 54: 2243-53.